

Distance Estimation to Support Assistive Drones for the Visually Impaired using Robust Calibration

Suman Raj, Bhavani A Madhabhavi*, Madhav Kumar^{†*},

Prabhav Gupta^{†*}, and Yogesh Simmhan

Department of Computational and Data Sciences,
Indian Institute of Science, Bangalore 560012 INDIA

Email: {sumanraj, simmhan}@iisc.ac.in

Abstract

Autonomous navigation by drones using onboard sensors, combined with deep learning and computer vision algorithms, is impacting a number of domains. We examine the use of drones to autonomously assist Visually Impaired People (VIPs) in navigating outdoor environments while avoiding obstacles. Here, we present NOVA, a robust calibration technique using depth maps to estimate absolute distances to obstacles in a campus environment. NOVA uses a dynamic-update method that can adapt to adversarial scenarios. We compare NOVA with SOTA depth map approaches, and with geometric and regression-based baseline models, for distance estimation to VIPs and other obstacles in diverse and dynamic conditions. We also provide exhaustive evaluations to validate the robustness and generalizability of our methods. NOVA predicts distances to VIP with an error $< 30\text{cm}$ and to different obstacles like cars and bicycles with a maximum of 60cm error, which are better than the baselines. NOVA also clearly out-performs SOTA depth map methods, by upto $5.3\text{--}14.6\times$.

1 Introduction

There is a growing trend for fleets of Unmanned Aerial Vehicles (UAVs), also called drones¹, being used for food delivery, flying ambulances [1], urban safety monitoring, and disaster response [2]. UAVs have become popular due to their agility in urban spaces and their lightweight structure. Further, autonomous navigation of UAVs is made possible by the integration of sensors such as GPS,

*were with Dream:Lab at the time of writing this paper.

[†]Equal Contribution

¹We use the terms UAVs and drones interchangeably in this paper.

cameras, accelerometers and LIDAR that help the drone perceive and understand its environment [3]. While LIDAR and depth cameras are commonly used for Simultaneous Localization and Mapping (SLAM) in UAVs [4], recent advances in Deep Neural Networks (DNN) models and Computer Vision (CV) algorithms, are enabling the use of monocular video streams from onboard cameras available in even low-end drones to achieve situation awareness and make autonomous navigation decisions, such as avoiding obstacles or navigating to a destination [5]. Further, advances in GPU edge accelerators and 4G/5G communications make it feasible to perform such real-time inferencing over video streams using onboard accelerators and/or remote cloud servers [6].

1.1 Motivating Application

While numerous applications of drones using autonomous navigation exist, we are exploring the use of drones as an assistive technology [7,8]. According to the World Health Organization (WHO) over 2.2 billion people suffer from moderate or severe visual impairment worldwide, of whom 36 million are blind [9]. This has a severe impact on their quality of life and can lead to social isolation, difficulty in mobility, and a higher risk of falls. We examine the use of drones to assist *Visually Impaired People (VIPs)* navigate outdoors, thus helping them lead an active urban lifestyle [10].

Among contemporary technologies for navigation assistance of VIPs, smart canes [11] and smart wearables [12,13] offer sensor and video-based guidance but suffer from a restricted range and Field of View (FoV) that limits the detection of hazards. Recent studies are exploring drone-based solutions. Nasralla et al. [14] examine the potential of CV-enabled UAVs to aid VIPs in a smart city. *DroneNavigator* [15] employs drones for VIP navigation using a digital (Bluetooth) and a physical leash, while Zayer et al. [8] utilize rotor sounds to guide VIPs in a controlled setting, with a human manually flying the drone. *Ocularone* [10] proposes the use of heterogeneous UAVs to guide VIPs in outdoor environments, using camera-based sensing and demonstrates situation awareness using a hardware prototype.

In this article, we focus on the specific and novel challenge of developing *CV-based methods over monocular drone video streams to accurately estimate the distance from the drone to the VIP, and to other potential obstacles*, to support such VIP navigation assistance applications.

1.2 Challenges and Gaps

Monocular cameras inherently lack true depth perception, which is a fundamental limitation for estimating the absolute distance from the drone to the object. Monocular vision-based algorithms are sensitive to the pose and geometry of objects due to the 2D projection of a 3D scene [16]. This is particularly true for objects with non-standard or irregular shapes, where edges and contours in 2D do not directly map to actual 3D boundaries. Monocular vision techniques are often unable to accurately resolve these ambiguities without additional depth

information [17, 18]. State-of-the-art (SOTA) methods, such as MiDaS [19] and Monodepth2 [20], generate a *monocular depth map* (Fig. 1b) using DNN models from a video frame. However, they only provide relative distances for the pixels of the objects in the image rather than the absolute distances. While they, and others ZoeDepth [21], offer methods to scale and shift parameters to retrieve the distances from the pixel scores, these are highly biased towards their training data and do not generalize. Also, some methods [19] exhibit higher errors at longer ranges or in poorly or harshly lit conditions [22], them unreliable in certain environments.

Others [23] have proposed an obstacle detection algorithm for monocular camera in UAVs by analyzing the change in the pixel-area of the approaching obstacles. Lee, et al. [24] use deep learning models for monocular obstacle avoidance for UAVs, specialized for navigating among trees in a plantation, and classify obstacles as critical or low-priority based on the height of the bounding boxes of the detected obstacles (trees). These geometric cannot be generalized to estimate the absolute distances to the objects required for VIP navigation, and require more robust based methods that map the height of these bounding boxes to absolute distances accurately.

Lastly, given the constrained computing power of drones, despite the use of edge accelerators, methods [25, 26] that require complex-calculations for each pixel in the frame can be intractable for real-time decisions.

1.3 Proposed Approach

To address these gaps, we present a novel approach for robust calibration for distance estimation, which we refer to in short as “NOVA” in the rest of the paper.

NOVA² is a generalizable method to estimate distances for any object in the frame, using depth maps and object bounding-boxes from DNN models. We propose strategies for score normalization and depth parameter estimation that translate the relative distances in depth maps into an accurate distance estimation to diverse objects near the VIP, using limited ground truth knowledge. Hyperparameters of NOVA trained on one person generalize well to others, and to other objects in the scene. It also uses recalibration to adapt to different ambient lighting and adversarial conditions, such as VIP image being cropped. We also use pixel sampling techniques within object bounding boxes to avoid costly computing on all pixels, and offer robustness to non-standard object orientations and unusual geometries.

We also propose two other data-driven approaches for distance estimation as baselines. First, is a **regression**-based supervised model that uses outputs from an object detection model and fits a linear equation to estimate the distance based on prior training data. This acts as a robust baseline for the VIP alone, and is used to recalibrate NOVA under dynamic scenarios. Second, is a **geometric** model that estimates the distance to the VIP and to other objects

²The term NEO is being used in all figures and plots to present results from NOVA.

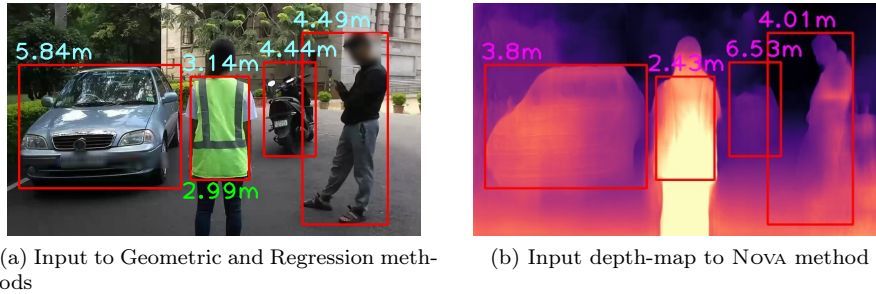


Figure 1: Distance estimation using proposed techniques.

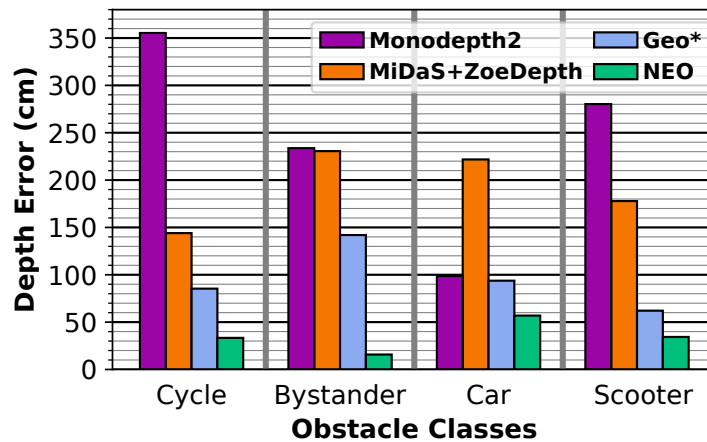


Figure 2: Comparison of NOVA and Geo* with SOTA depth map approaches for depth estimation using monocular drone camera.

using a pinhole camera model, homogeneous transformations, and the outputs from the object detection model. These approaches are visualized in Fig. 1, where *Regression* accurately estimates a distance of 2.99 m to VIP standing at a ground truth distance of 3 m but is limited to just VIPs. NOVA estimates a shorter distance to the VIP at 2.43 m, but performs better than Geometric for other objects and reports more accurate distances of 4.01 m to bystander and 3.8 m to car compared to higher values by the other method, while the respective ground truth distances are 4 m and 4.6m respectively.

1.4 Representative results of NOVA against SOTA methods

We briefly report the performance of NOVA relative to other State-of-the-art (SOTA) depth map-based approaches for monocular distance estimation and one

of our proposed baselines, Geometric* (*Geo**), over a larger set of drone video feeds. For the SOTA approaches, we use MonoDepth2 [20], and MiDaS [19] combined with ZoeDepth [21]. Monodepth2 provides a script to estimate the real depth using the Eigen split KITTI dataset [27] for calibration and generates a median distance-scaling value of 33.26, which we use to obtain the absolute distance. ZoeDepth introduces metric bin modules for specific domains (e.g., indoor or outdoor) that compute per-pixel depth bin centers and are fine-tuned to predict metric depth using real-world measurements. MiDaS’s decoder is hooked into the metric bins module of ZoeDepth to get the absolute distance. As we discuss later, NOVA adapts Monodepth2 using robust depth averaging and dynamic calibration.

Fig. 2 compares the absolute median depth error (in cm) using 3000 images of objects we have collected in our university for individual objects present in the drone’s FOV when for the respective classes. We report results for four common classes returned by the YOLOv8 model we use for object detection – bystander (person who is not VIP), cycle, scooter and car. The objects are 2–4 m from the drone. NOVA has the least error of 60 cm for cars and goes as low as 16 cm for a bystander. This is up to $5.3\times$ better than *Geo**, $14.3\times$ better than MiDaS and up to $14.6\times$ than Monodepth2. The high depth errors, sometimes running into meters, make these alternatives impractical for guiding VIPs to avoid obstacles.

1.5 Contributions

We make the following key contributions in this article:

1. We define the problem of estimating the absolute depth from the drone camera to objects in the scene using monocular depth maps to support the needs of VIP navigation (§ 2).
2. We introduce two light-weight baseline approaches to solve this: a supervised regression-based learning method, and a geometric method based on a pinhole camera model, using limited ground-truth information (§ 3).
3. We propose NOVA, a generalizable and compute-efficient method to estimate distances to any object in an image frame using the monocular depth map for the scene (§ 4). We further develop robust calibration techniques for NOVA to handle dynamic and adversarial conditions for VIP navigation.
4. We collect diverse ground truth dataset in our university campus that captures different object classes for static and dynamic scenarios (§ 5.3), which is used to perform a rigorous evaluation of the different methods. These illustrate their relative accuracies and robustness, and also their limitations (§ 6).

We also offer a detailed comparison our work with literature in § 7 and offer our conclusions and future work in § 8.

To the best of our knowledge, NOVA is the first work that offers a lightweight and generalized approach to estimate absolute distances to objects in the image frame captured using a monocular camera using a data-driven approach.

2 Problem Statement

We first describe the geometric model for the drone and VIP environment to help define the different distance-measures in our navigation model. We consider a 3D volume with dimensions h, d, w , where h is the height of the drone from the ground, d is the longitudinal distance of the drone from the VIP, and w is the width of lateral free space that the VIP requires for unobstructed motion (Fig. 3). h' is the vertical offset between the top of the VIP with height h'' and the current height of the drone. For simplicity, we assume that the orientation of the drone with respect to the VIP is fixed, and the heading of the VIP coincides with the heading of the drone.

2.1 Relative Positioning of the Drone

The height offset (h') and the distance (d) of the drone relative to the VIP is chosen such that the VIP is always in the FoV of the drone’s onboard camera. If f is the FoV of the camera, we can ensure that at least the top of the VIP’s head is visible to the drone by setting the offset and height as:

$$\tan\left(\frac{f}{2}\right) = \frac{h'}{d} \quad (1)$$

This however is not adequate for accurate tracking of the VIP for two reasons: (1) There is a variability of speed of the VIP during the movement, which requires a range to be set, and (2) the drone needs to capture a significant portion of the VIP height to be able to follow them with these variations. Instead, we define a range of valid values for $h' \in [h'', h_{max}]$ and $d \in [d_{min}, d_{max}]$, such that we have a straight line with coordinates $(h'', d_{max}), (h_{max}, d_{min})$ satisfying Equation 1. We set h_{max} and d_{min} as the point on the straight line where roughly *two-thirds* of the person starting from head is visible to the drone. We consider d_{max} as the farthest distance the drone can go behind the VIP such that it can detect obstacles up to a minimum distance d' ahead of the VIP. For practical purposes, we bound the values of $d_{min} \geq 2\text{ m}$ and $d_{max} \leq 4\text{ m}$ to stay within safe proximity limits.

2.2 Visibility Ahead of the VIP to Detect Obstacles

Since our work focuses on human-in-the-loop paradigm, it becomes crucial to estimate distances to all the objects in the frame which is within a tunable *safety-margin distance* (d') on the path directly ahead of the VIP that needs to be obstacle-free while they navigate. This is necessary for a smooth navigation experience for the VIP [28].

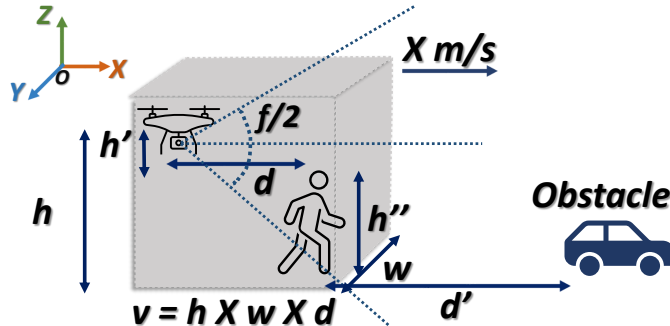


Figure 3: Illustration of different distances involved in our model

This depends on multiple factors such as: (i) *detection time* of the obstacle, between the camera observing it in its video frame to the processing of the frame using DNN models to identify the obstacle, (ii) *human reaction time*, which is the average time required for the VIP to comprehend and respond to an audio/sensory cue from our system when notifying them of an obstacle, and (iii) speed at which the VIP is walking (x m/s). Again here, based on our practical experiments, we set two distance-ranges for d' . Objects ≤ 1.5 m from the VIP, which can pose an imminent danger to the VIP, and objects between 1.5–5.5m from the VIP are with a lower risk.

Using the above setup, we define our problem statement as: “*Accurately estimate the distance from the drone to the VIP and to other objects present in the monocular video feed from the front-facing drone-camera, when the drone is following the VIP from a distance d and a height h from the ground, with priority given to nearby-objects.*”.

3 Distance Estimation using Baselines

The input to all our models is the video frame image from the drone camera annotated with the list of bounding boxes and classes for objects (including the VIP) present in the frame, generated by an object detection DNN model such as YOLO [29]. We initially propose two CV-based methods as the baselines for estimating the distance to a VIP (d_V) given a *video frame* of the scene and the *bounding box of the detection of the VIP* within that image (Fig. 1a). This is then extended to distance estimation to other objects in the frame.

3.1 Regression-based Model for VIP

Here, we adopt a supervised learning method where the ground-truth distances (d^i), from the drone to the VIP for several video frames (i) recorded at different static distances (d_V), are known. We train a linear regression model on the input features of the VIP detection bounding box: *width* (w_b^i), *height* (h_b^i), and



Figure 4: Workflow for distance estimation using Regression-based Model

Table 1: Training and Testing Dataset for Regression Model

| d_V (in m) | # Training Images (i) | # Testing Images |
|--------------|---------------------------|------------------|
| 2 | 893 | 597 |
| 2.5 | — | 590 |
| 3 | 921 | 589 |
| 4 | 963 | 594 |

area ($A_b = w_b^i \times h_b^i$), detected for the VIP in each frame i .

$$d^i = a \cdot w_b^i + b \cdot h_b^i + c \cdot A_b^i \quad \forall d^i \in d_V \quad (2)$$

We solve this over different frames i collected at different distances to get the coefficients a, b, c which are calibrated for the specific VIP and the drone camera. Subsequently, given the bounding box features of a VIP for an unknown distance d , we can solve this equation to obtain the distance d to the specific VIP. We refer to this method as *Regression*, as illustrated in Fig. 4.

We evaluate two variants: one trains the linear regression model using all 3 features while another uses just w_b and h_b as features. We validate the performance of both models on the training and testing dataset summarized in Table 1, whose d_V distances fall in the range of expected distances between the drone and the VIP. Fig. 5 compares the accuracy of the predictions using the *Absolute Error (in cm)* for each distance range. The model with 3 features has a tighter distribution and an overall median error of 27.2 cm compared to the one trained with just 2 features, which has a median error of 40.9 cm. It is considerably better for $d_V < 3$ m and comparable in accuracy for $d_V \geq 3$ m. Hence, we adopt the 3-feature regression model in subsequent sections.

Later, we show that this model works well when calibrated to a specific VIP, but is not generalizable for distance estimation to other objects since it is impractical to obtain the ground-truth bounding box features at known distances for a large class of objects, required to train the regression model.

3.2 Geometric Model

A pinhole camera model (Fig. 6) captures the geometry of an object in the real world projected by the camera lens onto the image plane [30]. Using basic geometric transformations, we can determine the distance between the VIP

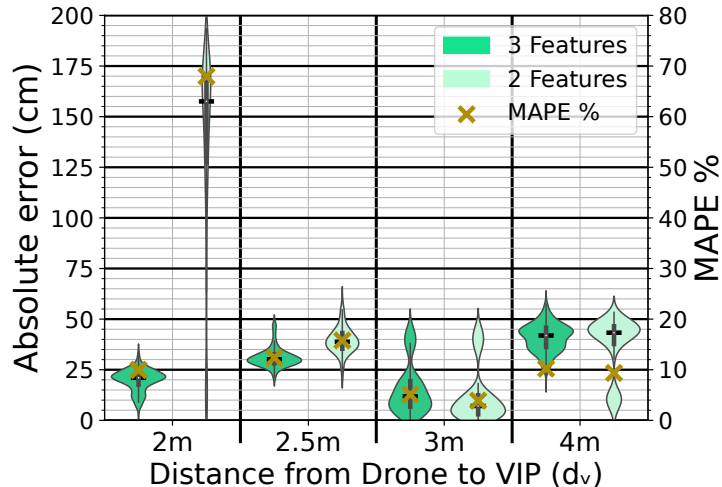


Figure 5: Performance of Linear Regression models for VIP distance estimation.

(vest) and the drone (camera lens), given the pixel height of the vest, the actual height of the vest, and the focal length of the lens, while accounting for the coordinate systems of the real world, image plane and object detection DNN model.

Let \mathcal{O}_w be the origin of the world coordinate frame (W) and \mathcal{O}_c be the origin of the camera coordinate frame (C). In Fig. 6, we assume that \mathcal{O}_w coincides with \mathcal{O}_c , and is at the pinhole (camera lens, shown by a white circle in center plane). Then, the object in the real world with a height of y_w meters (red upright line on left) is projected and inverted by the camera lens onto the image plane of the camera with a pixel height of py_c (red inverted line on right). The horizontal offset along the X axis and the distance from the lens are x_w and z_w for the real-world object and px_c and f_c for its projected image, where f_c is the focal length of the camera. z_w is the *distance to be estimated* from the drone to the vest.

The image plane is centered at F_c and the image has a height h and width w in pixels. However, the object’s bounding box returned by the object detection model uses the top-left corner of the frame as its origin, F_{dnn} . Hence, the pixel coordinate (px_{bb}, py_{bb}) relative to F_{dnn} is converted to a pixel coordinate (px_c, py_c) relative to camera F_c :

$$px_c = (px_{bb} - \frac{w}{2}) \quad py_c = -(py_{bb} - \frac{h}{2}) \quad (3)$$

Next, we generalize to the camera being at an elevation from the world coordinate since the drone is flying. We adopt the common convention [31] where the Z-axis of the camera coordinate frame is aligned on the negative Z-axis of the world coordinate. If h_d is the height of the drone (Fig. 6 Inset), \mathcal{O}_c translates h_d

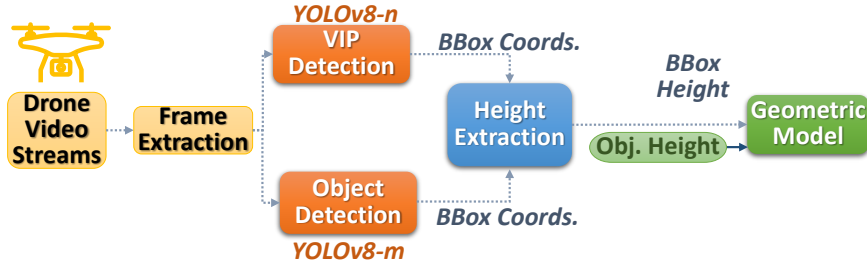


Figure 7: Workflow for distance estimation using Geometric Model

Similarly, the height of the image of that object is $h_i = (py_{bb1} - py_{bb2})$. On projecting h_o in W as h_i on the camera focal plane in C , we get the equation to calculate z_w , the real-world distance from the object (e.g., VIP’s vest) to the camera (drone) as:

$$z_w = f_c \times \frac{h_o}{h_i} \quad (8)$$

During calibration of the geometric model (Sec. 5.4), we provide the height of the object, their bounding box features, and the focal length of the camera – found experimentally or provided from the drone data sheet. Then, for any given object in the scene with a known real-world height h_o and a bounding box height h_b , we fit them into Eqn. 8 to calculate their distance from the drone, d . We show this using Fig. 7.

We have two variants of this method based on the value of h_o provided: (a) *Geometric* that uses average height estimates for an object class from a lookup table, and (b) *Geometric** that uses actual height of the object which is being captured by the camera of the drone. The former is easier to get for a larger class of objects while the latter is specific to heights of individual instances of the object, which is harder to secure.

Since Tello’s specifications does not provide focal length f , and instead gives a Field of View (FOV) of 82.6° , finding the focal length from the FOV is cumbersome. So we experimentally calculate f_c using Eqn. 8 from several reference images collected by the drone. Specifically, we extract ≈ 1000 images from a short video where Tello flies at a height of 1.5 m and is at a constant distance of 3 m from the VIP. The vest’s height is given as 0.63 m . This gives us a distribution of the focal lengths over 1000 images, which we find is bounded between quartiles, $Q1 = 1538$ and $Q3 = 1610$ pixels. We use the median focal length, $Q2 = 1592$ pixels, in subsequent sections. We confirm that this estimation works equally well for images at different drone heights and distances from the VIP.

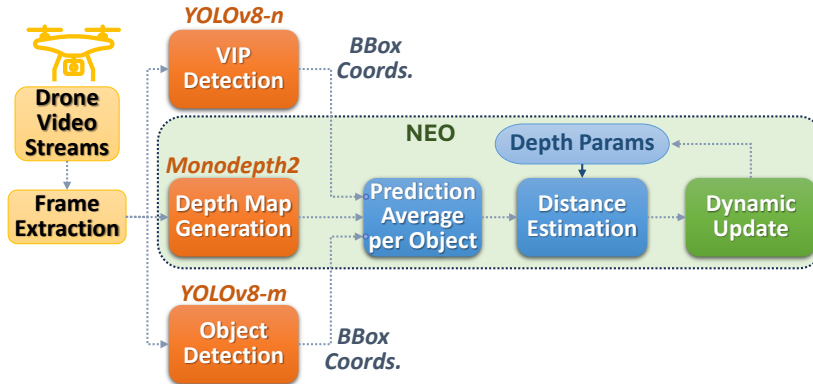


Figure 8: Workflow for distance estimation using NOVA

4 Distance Estimation using NOVA

Here, we propose a distance estimation approach, NOVA, leveraging recent works on *depth maps* using DNN for monocular images [16, 19, 20]. Depth map DNN models score each pixel in a frame such that pixels estimated to be at the same depth have the same score. There exists some transformation function from the score to the real-world distance to the object represented by that pixel, but this needs to be discovered through calibration. NOVA performs this calibration by using: (i) a video frame with the VIP, (ii) the distance to the VIP in the frame provided as ground truth ³, and (iii) the depth map for that frame from some DNN model. This calibration serves as the transformation function for the depth map, which converts the pixel scores to the real-world distance. Importantly, once calibrated, we can also use this function to find the distance to any other object in depth maps from the same DNN model generated for other frames from the same camera. Figure 8 illustrates the building blocks of NOVA, which we describe next.

4.1 Choice of Depth Map DNN Model

We first need to choose our base DNN model that generates depth maps using monocular images. Monodepth2 [20] uses a standard, fully convolutional, U-Net to predict the depth and uses techniques such as per-pixel minimum reprojection loss, auto-masking stationary pixels, and multi-scale estimation to improve self-supervised depth estimation for stereo as well as monocular images. We have also explored alternate models such as Adabins [32], U-Depth [33], Marigold [34], MiDaS [19] and DenseDepth [35]. However, only Monodepth2 and MiDaS exhibit a monotonic trend in depth scores when the distance of objects from the

³This can either be captured using a LiDAR or calculated using the geometric and/or regression model baselines.

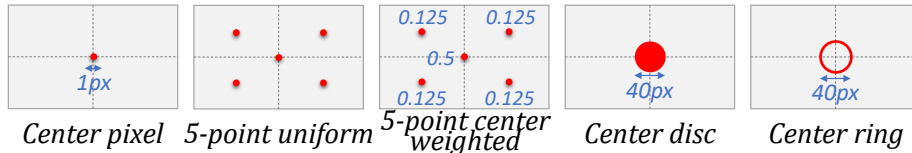


Figure 9: Depth score normalization techniques for an object’s depth map.

camera changes. Among these two, Monodepth2 is more reliable and we choose it as our base DNN depth map model.

Monodepth2 generates scores indicating the relative inverse depth for each pixel in a frame. The absolute depth for a score is:

$$d = m \cdot score + s \tag{9}$$

where m and s are the *scale* and *shift* depth parameters, and d is the real-world distance to the object. We extract frames from the drone video, downscale them from a resolution of 1280×720 p to 1024×320 p required by Monodepth2, and get the depth map for the scaled video frame. We correspondingly scale and overlay the bounding boxes reported for the objects in the frame, and extract the depth map images for each object within these bounding boxes. This gives us depth values for each pixel within the bounding box for the object. We then perform depth score normalization, as discussed next.

4.2 Depth Score Normalization per Object

The depth map scores for the pixels within an object can vary significantly within the bounding box, e.g. due to the object having a complex shape, non-uniform depth, lighting conditions, etc. We propose and evaluate several normalization techniques (Fig. 9) to determine a single representative depth score for the object that is used to ascertain the actual depth for it using the calibration model.

The simplest normalization method is to select the *center pixel* of the bounding box as the representative pixel. But this can skew the results for complex objects if this pixel happens to fall on some background behind the object. We mitigate this selecting 5-points at the center of the box and at the center of each quadrant of the box, and weighing them equally (*5-point uniform*) or giving higher weight to the center pixel (*5-point center-weighted*). Expanding on this, we can take the average of the depth scores of pixels within a *disc at the center* of the box to avoid single-pixel errors, or average the circumference of this disc to give *center ring*, e.g., of diameter 40px. However, the center of the object is not necessarily the nearest portion of that object from the camera. At the other end, we can also find the *median* or *mean* of the depth scores across all pixels in the bounding box. Lastly, we take an average of the the lowest 10%ile of the pixel depth scores in the bounding box and uses this as the score for the object, called *Low Threshold (LT)*.

Our evaluations show that LT normalization technique performs the best for our VIP usecase for different classes and shapes of objects. E.g., for a bicycle placed at $3m$ distance from the camera, the distances reported are $3.23m$, $5.19m$, $6.37m$, $3.85m$, $4.62m$ and $3.16m$ using the center pixel, 5-point center-weighted, 5-point uniform, disc at the center, center ring and LT methods, respectively. We also find LT to be robust to complex shapes of relevant objects since it considers the pixels *nearest* to the drone which are the ones that will form the immediate obstacle to the VIP, e.g., for a car where the bottom half is likely to be protruding and hence closer to the drone than the top half, this normalization strategy helps us estimate the distance to the bottom (nearest) half of the car. Hence, we use LT for subsequent experiments. As we discuss later, we complement this with a sliding window averaging technique across frames in a video to smooth out the changes in the normalized score.

4.3 Estimation of Depth Coefficients for Calibration

Intuitively, we need just 2 pixel scores and their real-world distances to calculate the scale (m) and shift (s) calibration coefficients in Eqn. 9. These can be obtained by taking two frames with the VIP present at two different known distances, and using their normalized depth scores. However, we find that the accuracies are highly sensitive to the specific video scenes from which the frames are chosen, the lighting conditions and the distances to the VIP.

We perform this calibration using video collected for the VIP at 6 different distances from the drone, and select different distance pairs to perform the fit: $D = \{(2m, 3m), (2m, 3.5m), (2m, 4m), (2.5m, 3.5m), (2.5m, 4m), (3m, 4m)\}$. These pairs are chosen such that the difference in distances for each is $\geq 1m$, to cover sufficient spatial region. Then, using images from videos of the VIP collected at each distance pair, we fit Eqn. 9 to return a distribution of values for m and s ; among these, we choose the median value of m and s to ensure consistency.

We evaluate these different calibration coefficients using test video frames where the same VIP stands at different distances from the drone and in different background/lighting conditions. We then choose the best combination of m and s from them based on the lowest sum of absolute median errors and the lowest sum of positive and negative median errors. This is empirically evaluated in § 5.4.

4.4 Dynamic Recalibration of Depth Coefficients

Depth maps can be affected by lighting and ambient conditions, as these factors affect the quality and accuracy of visual features captured by the camera. Changes in lighting can cause inconsistencies in feature extraction, while varying environmental conditions, such as sunlight, shadows, or reflections, can distort depth estimations. Such challenges are especially critical in dynamic outdoor settings, where the scene characteristics are constantly evolving. This can cause

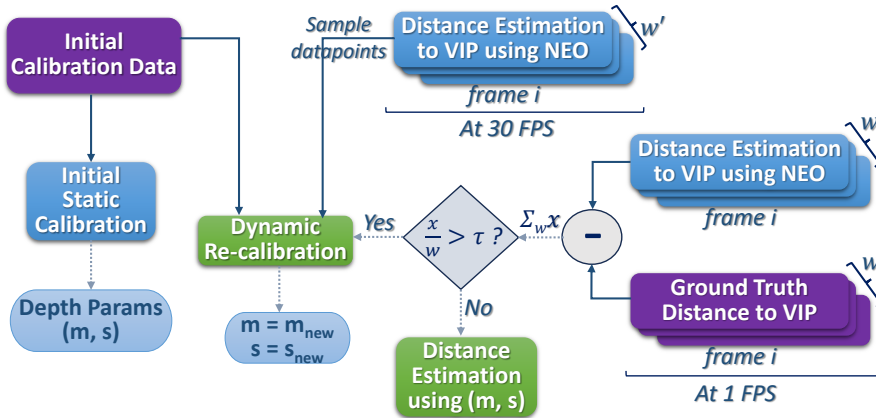


Figure 10: Dynamic Re-Calibration of Depth Parameters

discrepancies between the expected and observed depth values beyond a threshold. This indicates that the current calibration no longer works for the outdoor setting, and a recalibration is required.

While the initial calibration was done offline, these ambient changes require recalibration to be done dynamically to suit the changing scenes as the VIP is moving. NOVA proposes a novel mechanism relevant to the VIP scenario where it leverages the fact that the regression method is accurate for VIP distance estimation under diverse conditions, and this can be used for detecting and calibrating NOVA’s depth maps and re-estimate their depth coefficients m and s . We outline this using Fig. 10.

Intuitively, this is done in two steps. In the first step, NOVA detects inaccuracies by comparing its estimated distance against the ground truth distance for the VIP over a sliding window of frames. Recalibration is triggered if the error exceeds a threshold τ . During recalibration, depth coefficients are updated by combining recent frames data with initial data, balanced by a tunable parameter α . While the detection and recalibration process is based on the VIP’s image, the recalibrated parameters are used for all objects. This helps ensure robust and accurate distance measurements across the scene. Next, we discuss these steps in detail.

4.4.1 Detection

We first decide if the existing coefficients need to be re-calculated for a given video scene. We compare the accuracy of the distance estimation to the VIP given by NOVA, relative to the (more reliable) distance estimate to VIP from *Regression* or *Geometric* models, or any other source of ground truth. We maintain a sliding window over the VIP image frames at 1 FPS, with a window duration w seconds, which stores the depth predictions to the VIP by NOVA (d_{NOVA}) and by a ground truth model (d_G). If the average absolute distance

Algorithm 1 Dynamic Recalibration of Depth Coefficients

```

1: function RECALIBRATE( $w, w', \alpha, n_o, n_{new}, n_{orig}, \tau$ )
2:    $\triangleright w$  and  $w'$  are the window sizes of the sliding windows over the VIP images
   at 1 FPS and 30 FPS respectively.  $n_o$  is the number of frames in  $n_{orig}$  and  $n_{new}$ 
   is the number of data points sampled from the recent  $w' \times 30$  frames.  $\alpha$  is the
   weight given to the original parameters
3:   Initialize  $R[\ ] = 0, D[\ ] = 0$  and  $T[\ ] = 0$   $\triangleright$  Initialize regression buffer,
   depth buffer as empty list of size  $w$  and train buffer depth as empty lists of size  $w'$ 
4:
5:   Initialise  $\text{flag} = 0, i, j = 0$ 
6:   for each new image do
7:     if  $j < 5$  then
8:        $R[j]$ .append( $d_G$ ) at 1 FPS
9:        $D[j]$ .append( $d_{\text{NOVA}}$ ) at 1 FPS
10:       $T[(j \times 30) + 0 \dots (j \times 30) + 29]$ .append( $d_G$ ) at 30 FPS
11:     else
12:       if  $\text{flag} == 0$  then
13:          $i = j \% w$ 
14:          $R[i] = d_G$  at 1 FPS
15:          $D[i] = d_{\text{NOVA}}$ 
16:          $T[(j \times 30) + 0 \dots (j \times 30) + 29] = d_G$  at 30 FPS
17:       end if
18:     end if
19:
20:     if  $\frac{\sum_{i=(0,w)} |d_G^i - d_{\text{NOVA}}^i|}{w} > \tau$  then  $\triangleright$  Detection
21:
22:        $\text{flag} == 1$ 
23:     end if
24:     if  $\text{flag}$  then  $\triangleright$  Re-computation
25:       Calculate  $n_{new} = \frac{n_o}{\alpha} - n_o$ 
26:       Sample  $n_{new}$  data points from T and append to  $n_o$ 
27:       Perform linear fit over  $n_{orig} + n_{new}$  samples
28:     end if
29:      $j+ = 1$ 
30:   end for
31: end function

```

Table 2: DNN Models and Performance on Orin Nano

| Application | DNN Model | Infer. time/frame (ms) |
|---------------------|-------------------|------------------------|
| VIP Detection | RT YOLO v8 (nano) | 35 |
| Object Detection | YOLO v8 (medium) | 68 |
| Monocular Depth Map | Monodepth2 | 15 |

error over this window using NOVA exceeds a certain threshold τ , we trigger a recalibration of the depth coefficients.

$$\frac{\sum_{i=(0,w)} |d_G^i - d_{\text{NOVA}}^i|}{w} > \tau \quad (10)$$

This approach ensures that the recalibration is only triggered when necessary. By using a sliding window to track errors over time, it captures persistent inaccuracies rather than any transient noise, and hence ensures a robust and adaptive performance in dynamic environments.

4.4.2 Recalibration

Once NOVA detects the need to re-calibrate, it triggers the process to adjust the depth coefficients, as shown in Algorithm 1. Towards this, we additionally maintain a sliding window of the VIP frames at 30 FPS with a window duration of w' seconds, which stores the normalized depth scores and the ground truth distances to the VIP. We also store the depth scores and their ground truth distances to the VIP for the n_o original frames collected from the “best” distance-pairs used when initializing the coefficients (§ 4.3).

We then calculate $n_{new} = \frac{(1-\alpha)}{\alpha} \cdot n_o$, where α is a tunable parameter, giving a weightage of α to the frames used to generate the original parameters and a weightage of $1 - \alpha$ to recent frames. We use this to sample n_{new} data points from the recent $w' \times 30$ frames and append them to the original set of frames, and redo a linear fit over the $(n_{orig} + n_{new})$ samples to recompute the updated m and s . This approach ensures a balance, allowing sufficient new data to influence the recalibration and account for recent environmental changes, while also preserving the generality offered by the original calibration data and preventing a skew towards only recent frames that may be a transient phase. We set the hyper-parameters w , w' , α and τ in Sec. 5.4, which are then used for evaluation.

5 Experimental Setup and Datasets

5.1 Implementation and Setup

The distance estimation approaches discussed above have been implemented in *Python*. We use *PyTorch v2.0.0* for invoking the various DNN models (Table 2) for inferencing over the video streams to generate outputs that feed into our

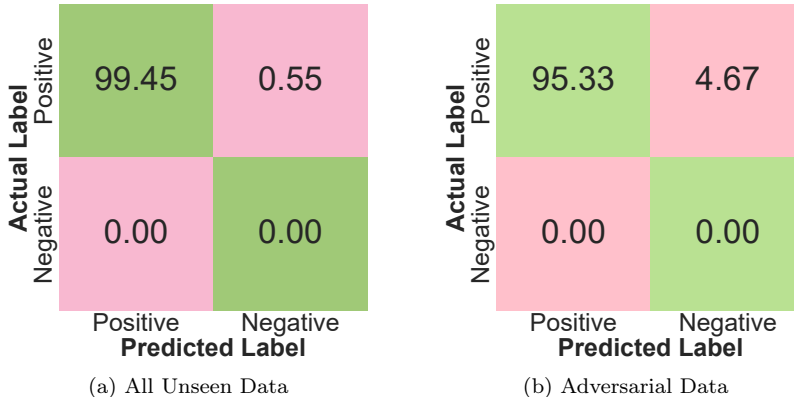


Figure 11: Accuracy (in %) of VIP detections using our Re-trained (RT) YOLOv8 (nano) model.

distance estimation and calibration models. Videos used in these experiments for training and testing are recorded using a *DJI Tello* [36] nano quad-copter, which weighs 80 g with battery and has an onboard 720p HD monocular camera that generates feeds at 30 frames per second (FPS). The frames are extracted using *moviepy* Python library. We use an *Nvidia Jetson Orin Nano* developer kit [37] as our accelerated edge device. It has a GPU with 1024 Ampere CUDA cores, 32 tensor cores, a 6-core Arm Cortex-A78AE CPU, and 8 GB RAM shared by CPU and GPU. It is 176 g in weight, $10 \times 7.9 \times 2.1$ cm in size and can be powered by a portable USB powerbank. It is compact enough to be carried by the VIP in their backpack or purse. Its inferencing times per frame for the DNN models we use are shown in Table 2.

We collect two categories of dataset: (a) images with VIP in different background at varied distances to train VIP detection DNN model (§ 5.2), and (b) images of different classes of objects and VIP at specific distances in managed scenes to evaluate our distance estimation models (§ 5.3).

5.2 VIP Detection Image Datasets and Model

5.2.1 Dataset Collection

We record a number of videos under managed and realistic settings inside our university campus using the Tello drone. A key prerequisite for distance estimation to the VIP from the drone is to first identify the VIP in the video frame, which serves to bootstrap other distance estimation models. The VIP wears a fluorescent green hazard vest as a unique visual marker, and was chosen from several other alternatives [10].

We collect and annotate a large data corpus of $\approx 30,000$ VIP images using the drone under diverse environmental conditions and lighting conditions. A



Figure 12: A proxy for VIP standing at $4m$ from drone’s camera depicting different scenes used for evaluation

student serves as a proxy for the VIP, wears the hazard vest and walks around our campus under different visual and physical conditions, with the drone following them. There are a total of 12 *scene categories*, e.g., walking on the pavement or the road-side, with and without pedestrians, etc. Some of these are adversarial conditions, like evening low light, green background with low contrast, etc. We manually annotate each video frame using Roboflow to assign bounding boxes to the VIP’s hazard vest. This unique labeled dataset will be made public at our GitHub page at anonymized upon acceptance of the article.

This serves as the ground truth for training and validation under normal and adversarial conditions, and helps evaluate the robustness of the approaches.

5.2.2 Training of VIP Detection DNN Model

This DNN model is used by all of our approaches as the initial step for VIP and object detection. We randomly sample 10% of the VIP data from each scene category to avoid overfitting the DNN model for a total of 3753 images. We split this into an 80 : 20 training and validation dataset to re-train YOLOv8 (nano) [29] and find the accuracy to be 99.4% on the remaining 90% (23, 543) of the unseen images (Fig. 11a), including a 95.3% accuracy on the adversarial data (3805 images; Fig. 11b). The output of this highly accurate DNN model, reporting the VIP detections as a bounding box, serves as the input to the distance estimation techniques that we have proposed. The detections returned by the model is the top-left and bottom-right (x, y) pixel coordinates of the bounding box of the vest, with the origin set at the top-left corner of the image frame. These are further used in our distance estimation models.

5.3 Distance Evaluation Video Dataset

We further collect videos of various real-life and managed scenes encountered by a VIP walking on our campus to use in our evaluations. The videos are recorded using the DJI Tello drone at a height of 1.5 m and at 30 FPS. These exhibit diversity along several dimensions for a realistic evaluation.

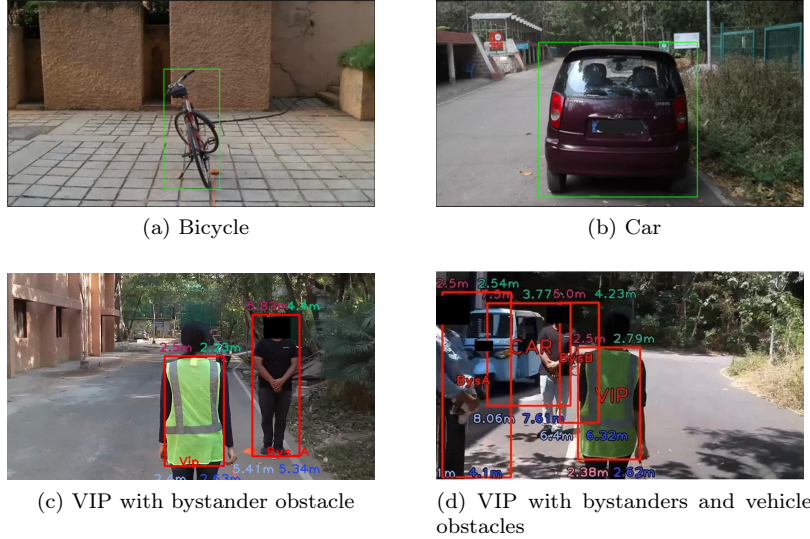


Figure 13: Frames from videos of obstacles dataset collected for evaluation

5.3.1 Static VIP Dataset

We collect the videos of the VIP in 3 different *scene settings*, where different VIPs (student serving as proxies) stand against different *backgrounds* and lighting when the drone is also stationary. The background/lighting conditions include: a plain light background in the morning (AM_Simple), a green foliage in the morning (AM_Complex), and a green foliage in the evening (PM_Complex), as shown in Fig. 12. These scenarios cover a wide range of simple and complex outdoor scenes that we encounter in the real world. For each scene setting, we record 10 seconds of video with the VIP at *distances* of 2–4m from the drone in steps of 0.5m. With three different VIP proxies, we have $3 \text{ VIP} \times 3 \text{ scene} \times 5 \text{ distance}$ combinations for a total of 450s diverse videos for VIPs, and $\approx 14.7k$ frames are extracted from these.

5.3.2 Static and Dynamic Obstacles Dataset

In order to evaluate our models on different outdoor objects, we first record videos with only a *single stationary obstacle* present in the frame. For each of the four obstacle classes in static scenarios: bystander, cycle, car and scooter, we have two class instances, e.g., an SUV and a hatchback car, different bystanders,

⁴These videos include the VIP in all frames as the drone followed them, but they are excluded from reporting since obstacles were the primary focus. Here, proximity from the drone refers to the initial distance, which decreases as the VIP moves closer to the obstacles.

⁵VIP count is reported only for videos with exclusive VIP frames. In videos containing both bystander and VIP, only bystander frames are reported.

Table 3: Summary of Distance Evaluation Video Dataset

| Categories | Total Video Length | Motion in Frame | Classes (Count) | # of Video Clips | Proximity from Drone | # Extracted Frames (FPS) |
|---------------------------------|--------------------|-----------------|-----------------|------------------|----------------------|--------------------------|
| VIP | 490 s | N | VIP (3) | 45 | 2-4 m | 14719 (30) |
| Obstacles | 400 s | N | Bicycle (2) | 10 | 2-4 m | 3300 (30) |
| | | | Car (2) | 10 | 2-4 m | 3154 (30) |
| | | | Scooter (2) | 10 | 2-4 m | 3146 (30) |
| | | | Bys. (2) | 10 | 2-4 m | 3010 (30) |
| VIP with Obstacles ⁴ | 590 s | Y | Bys. (3) | 4 | 5-73 m | 195 (1) |
| | | | Car (1) | | 4-65 m | 133 (1) |
| | | | Scooter (1) | | 17-62 m | 31 (1) |
| | | | Bicycle (1) | | 10-51 m | 64 (1) |
| Adversarial ⁵ | 42 s | Y | VIP (1) | 2 | 2.5m | 252 (30) |
| | | | Bys. (1) | | 1 | 2.5m |

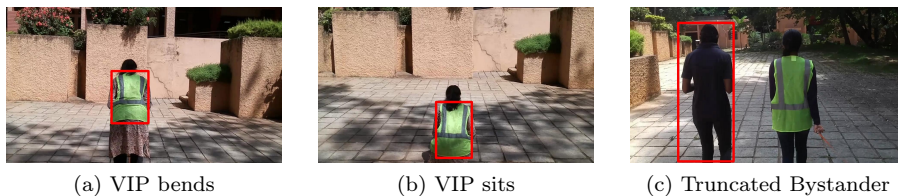


Figure 14: Adversarial images of VIP and bystander

etc., with different backgrounds, and at distances of 2–4 m from the drone in steps of 0.5 m. Samples images are shown in Fig. 13a and 13b. The combined duration of all these videos is 400s, and we collect ≈ 3000 validation images for each class.

Additionally, we collect videos where the drone follows the VIP at a distance of 2.5m, and different obstacle classes are encountered under diverse conditions, e.g., as shown in Fig. 13c and 13d. We separately measure the distances to the obstacles from the drone along this trajectory to get the ground truth distances. While these obstacles are stationary, their relative distances to the moving drone changes across the frames and are present in different backgrounds. We have 4 videos with a total duration of 590 seconds, from which obstacles data were extracted at 1 FPS and VIP data at 30 FPS. Bystanders, cars, scooters, and bicycles appeared in 195, 133, 31, and 64 images, respectively.

5.3.3 Adversarial Dataset

In addition, we also record ≈ 40 s of *adversarial scenarios* for the VIP and obstacles, e.g., where the VIP bends down, moves to the edge of the frame, etc. We show different adversarial scenarios for the VIP and a bystander: (a) VIP

bends (Fig. 14a), (b) VIP sits (Fig 14b), and (c) a bystander next to the VIP gets truncated (Fig. 14c).

The effort in collecting these diverse and complex videos spanned a couple of months, and will be made public. A summary of the datasets have been provided in Table. 3. In our evaluations, the focus is on detecting and classifying humans within video frames, rather than observing or analyzing their behaviors. Hence, we confirm that we are exempt from obtaining approval from institutional review board (IRB). Additionally, we have also obtained official consent from all individuals who have participated in our dataset, either as VIP proxies or bystanders, in accordance with ethical guidelines before their participation.

5.4 Calibration of Distance Estimation Models

Next, we apply the calibration approaches proposed earlier to the datasets we have collected to decide the relevant coefficients.

5.4.1 Regression model

This mode is only used to estimate distances to the VIP. Since this is specific to each VIP, we calibrate it for each individual VIP by sampling 10 frames from their AM_Simple videos at distances of $\{2m, 3m, 4m\}$ from the drone, i.e., a few seconds of the VIP’s videos at three distances is all that is required, imposing minimal one-time effort for the VIP–drone pair. Using this, we fit the linear regression Eqn. 2 and get the coefficients (a, b, c) . For the three VIPs in our datasets, these coefficients are: $(-2.42, -1.29, 0.0043)$ for VIP1, $(-2.14, -1.77, 0.0050)$ for VIP2, and $(-2.56, -2.10, 0.0065)$ for VIP3.

5.4.2 Geometric Models

The Geometric and Geometric* models can estimate the distances to the VIP and to obstacles that are present among the *80 known object classes* of YOLOv8 (medium). For calibration, we require the height h_o for that object besides the focal length f_c of the camera in Eqn. 8. In case of *Geometric*, this is the expected (average) object height, and for *Geometric**, it is the actual height for that specific object instance. The expected heights are sourced from public domain information is a one-time effort, while the actual height for an object is impractical to get in practice; we manually measure it for the datasets we collect and it serves as an “ideal” case for this model. In our study, the heights of the obstacle class instances in our videos are: Bystanders (expected=1.65m, actual={1.75m, 1.76m}); Scooters (expected=1.12m, actual={1.14m, 1.25m}); Bicycles (expected=0.97m, actual={0.95m, 1.18m}); Cars (expected=1.7m, actual={1.56m, 1.38m}).

5.4.3 NOVA model

Static calibration helps decide the *scale* (m) and *shift* (s) values for MonoDepth2 (§ 4.3), *a priori*, and is used for all subsequent scenes by NOVA. While we

calibrate using the VIP images (similar to regression), we reuse these coefficients to decide the actual depths to all objects in the videos – this re-usability is a key benefit of NOVA, unlike regression. Here, we select a pair of distances to the VIP, sample 10 images at these two distances from the `AM_Simple` videos, and use these to fit m and s in Eqn. 9. From our experiments using distances of $\{2m, 2.5m, 3m, 3.5m, 4m\}$, we find that the distance-pair of $(2.5m, 4m)$ offers the lowest average median errors across diverse samples. These two distances are far apart and able to capture the variability in the VIP distances. So, using 10 images at these two distances, we calibrate the coefficients for each of the three VIPs, and find the (m, s) values to be $(1169, 124.2)$, $(1685, 54.9)$, and $(1105, 118.5)$, respectively.

In *dynamic calibration*, we update the coefficients at “runtime” if the estimation error to the VIP using NOVA relative to the regression model exceeds $\tau = 30\text{cm}$ over a window of $w = 5$ frames; we evaluate different detection window sizes of $w = \{5, 10, 15\}$ and find 5 to be the best. If the error exceeds τ , we recalculate m and s over a sliding window of VIP frames over $w' = 5$ secs, with $\alpha = 0.75$ used as the weighing ratio; this was the best after evaluating $\alpha = 0.25\text{--}0.75$.

These parameters need to be *calibrated once* for a given drone camera. For *Regression* and NOVA, the camera can affect the bounding box reported by Yolo that are used for by these models. For the geometric model, the focal length of the camera needs to be manually computed or used from the datasheet for the camera.

6 Evaluation Results

We use the above calibrated distance estimation models, regression, geometric and NOVA, to evaluate the accuracy for the diverse set of validation videos that we have collected. We report and analyze these results here. Additionally, we present the results from the existing state-of-the-art (SOTA) methods, Monodepth2 and MiDaS + ZoeDepth, as outlined in § 1.4. These methods are briefly mentioned as they consistently perform worse than NOVA and our proposed baselines.

6.1 Robustness of distance estimation for VIP

First, we evaluate the accuracy and robustness of distance estimates to a *static VIP*. For this, we use the stationary VIP video datasets described in § 5.3.1, with varying VIPs, distances and backgrounds/lighting conditions.

Figure 15 reports the signed error (in cm) for the distance estimate to the VIP given by the *Geometric*, *Regression* and *NOVA* models, relative to the actual ground truth distance. We report $Error = (true\ value - predicted\ value)$; here, positive errors indicate an underestimate of the distance from the drone, while negative errors represent an overestimate. The combined bars for a method in a scene represent the error distribution across all three VIP video frames ($4.8k$),

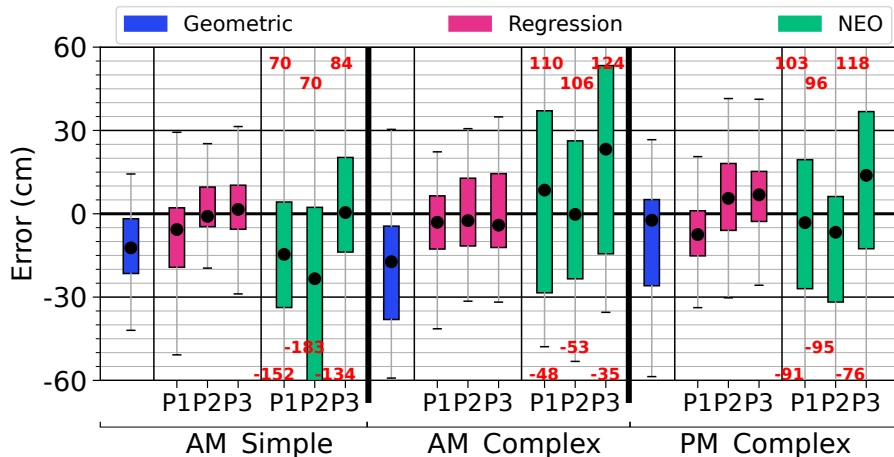


Figure 15: Accuracy of distance estimation for static VIP for simple and complex scenes.



(a) Vest cropped at bottom



(b) Shiny surface of a Car

Figure 16: Outlier images from VIP and Obstacles dataset

reported for each model. For Regression and NOVA, the models are calibrated for a specific VIP (P1, P2, P3), shown in the X axis, but validated across datasets from all VIPs to understand their generalizability.

Our *Regression* model (pink bars) provides the best distance estimation for VIP with a median error range of only -8cm to 7cm , irrespective of the VIP for which it was originally calibrated on. These models also have a tighter distribution. *Geometric* performs the next best with a median error between -18cm to -2cm , with the peak errors going up to -39cm . The higher error is caused by the hazard vest being partially cropped from the image when the drone is close to the VIP (e.g. 2m in Fig. 16a). This causes the height of the bounding box to reduce and results in an overestimate of the distance. *NOVA* has a maximum median error of $\pm 25\text{cm}$ but also has a higher variability. We observe the maximum variance to occur in the *AM_Complex* scene due to the bright sunlight reflecting off of the background and partially off of the VIP’s vest (e.g., Fig. 12b). This reduces during the evening, when the brightness is uniform for all pixels of the vest (e.g., Fig. 12c).

Finally, we evaluate the accuracy using SOTA methods. Monodepth2 achieves

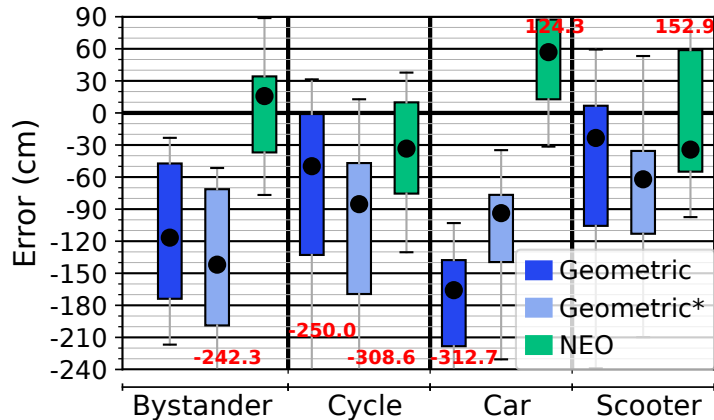


Figure 17: Accuracy of distance estimation for static obstacles.

an absolute median error (in cm) of 141, 174, and 162 for `AM_Complex`, `AM_Simple`, and `PM_Complex`, respectively. `MiDaS + ZoeDepth` achieves an absolute median error of 154, 174, and 196 for the same datasets. These numbers are excessively high and render the methods unsuitable for practical scenarios.

Discussion. Overall, the median errors for all strategies are within ± 30 cm error, our nominal tolerance level. Also, regression and NOVA models, despite being calibrated on one VIP, generalize well across different VIPs, showing comparable errors for P1, P2 and P3. However, the distance estimate to the VIP from the drone needs to be more accurate and robust than the ± 30 cm margin of safety we consider for other obstacles. This distance value is actively used for drone and VIP navigation, and will compound the distance errors to other obstacles. As a result, we adopt the Regression model, with a median error of ± 8 cm and the tightest error distribution, as our preferred VIP distance estimation model in subsequent experiments. While not shown, we also report that Regression offers the best accuracy even when the VIP and drone are moving, with a peak error ≤ 15 cm, while Geometric and NOVA have a peak error of ≈ 30 cm.

6.2 Robustness of distance estimation for static obstacles

Next, we validate the Geometric and NOVA models to estimate distances to obstacles in the vicinity of the VIP; Regression works only for the VIP and is omitted here. Here, we consider static scenes, i.e., neither the VIP nor the obstacles are moving; dynamic scenes are considered in the next section. We evaluate the models on the ≈ 3000 validation images for bystanders, cycles, cars and scooters with different backgrounds and distances introduced in § 5.3.2 and Fig. (13b,13a).

Fig. 17 reports the distance error for these static obstacles. For obstacle avoidance, *under estimates (positive errors) are better than over estimates (neg-*

ative errors) since it is better to take corrective measures assuming an object is closer than reality, than assume it is farther away and potentially collide, i.e., high *recall* is more important than high *precision*.

NOVA performs consistently better than the *Geometric* methods and exhibits a peak median error of 56cm for cars and falls within a median of 35cm for other obstacles. The pixel normalization used by NOVA over the depth map image (§ 4.2) ensures that it is robust to scenes where the images of the obstacles are cropped, unlike the *Geometric* method. NOVA, however, is susceptible to reflections from shiny surfaces (as seen before for the reflective vest), which it encounters in cars (e.g., Fig. 16b) and causes a positive error, and this increases with an increase in actual distance.

The *Geometric* model performs much worse as it is highly dependent on the entire image of the obstacle being visible. This often fails when the objects are nearby, *precisely when accurate estimates are important*. For an object, this ratio equality should hold: $\frac{h_o}{h_b} = \frac{d}{f}$. For the focal length of 1592 pixels for the Tello camera, this ratio translates to values of {0.12, 0.15, 0.19, 0.22, 0.25} for distances {2, 2.5, 3, 3.5, 4}m, respectively. However, for obstacles closer to the drone (and hence the VIP), cropping of the image and bounding box causes this ratio to not hold and the shorter (visible) height translates to an overestimate in the distances. E.g., cycles at closer distances of 3 → 2m have errors grow from 26 → 124%. Errors also amplify for taller objects, e.g., bystanders are cropped even at 3m and have 85% error.

Similarly, *Geometric* diverges from the idealized *Geometric** when the actual height of the object is higher than the expected height, or because of truncation. E.g., the median error increases by 39cm for *Geometric** compared to *Geometric* for scooter as its expected height is 112cm while the actual heights are 114cm and 125cm. In contrast, the error decreases by 72cm for cars, where average and actual heights are 170cm and 138cm. Lastly, we report the results from SOTA methods for static obstacles in § 1.4.

6.3 Distance estimation for dynamic obstacles

Next, we validate our models on realistic scenarios where the VIP is walking with the drone following, and various stationary obstacles are moving relative to the drone within the scene. We use the dataset introduced in § 5.3.2 and Fig. (13d,13c), with 133, 64, 31 and 195 video frames of car, cycle, scooter and bystander respectively. The ground truth distance between the drone’s initial position and these obstacles ranges from 4 – 73 meters. This distance decreases as the drone follows the VIP and gets closer to the objects. We limit our analysis to objects within 8 meters from the drone, and use the dynamic variant of NOVA here.

We report the *Average Signed Error (ASE)* to each obstacle class. We categorize the images into (i) objects ≤ 4m to the drone, which can pose an imminent danger to the VIP, and (ii) objects 4–8m from the drone with lower risk. These are represented using a matrix for each obstacle type in Fig. 18 whose outer quadrants show the *Average Signed Error (ASE)* for the objects

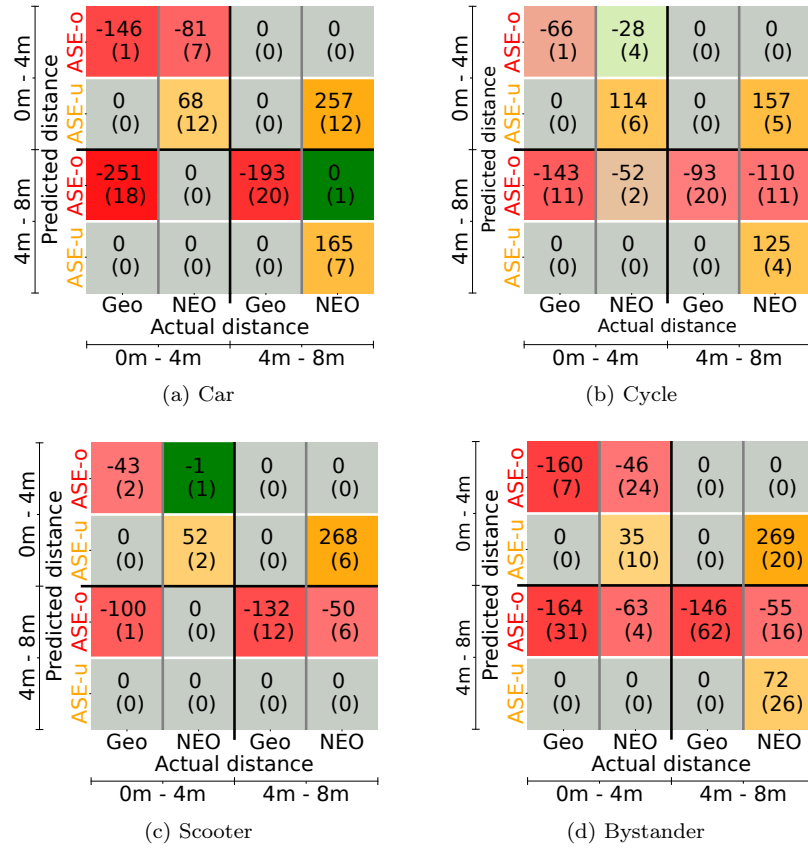


Figure 18: Matrix showing over- and under-estimation errors (ASE in *cm*) for NOVA and Geometric (inner quadrants), at $\leq 4m$ and $> 4m$ distances (outer quadrants), for obstacle types present in dynamic scenes. # of frames in each cell is shown in parentheses.

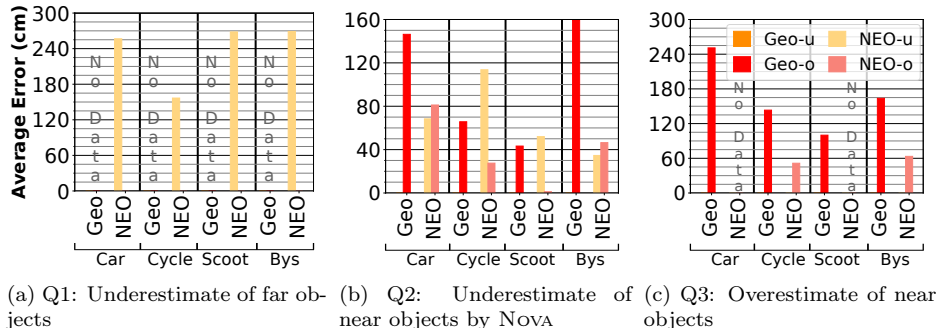


Figure 19: Per-quadrant analysis of over and under-estimates

at closer and farther distances, i.e., actual and predicted distances are $\leq 4\text{m}$ (Q2, top left quadrant), real is $\leq 4\text{m}$ but predicted is $> 4\text{m}$ (Q3, bottom left), etc. Within quadrant, we report $ASE-o$ and $ASE-u$ separately for Geometric and NOVA models, indicating over and under prediction errors. The number of frames in each category is shown in parenthesis for context. E.g., some may have 0 frames in that bucket (grey cells). Errors $\leq 30\text{cm}$ (green cells) perform the best. As before, we prefer lower $ASE-u$ under-predictions (yellow) to $ASE-u$ over-predictions (red), and also better predictions for closer objects than farther, i.e., errors in Q3 should be the least, then Q2, Q1, and Q4.

For *cars* (Fig. 18a), the Geometric model overestimates the distances for all 39 images while NOVA overestimates only for 7 of 39 images. For objects closer than 4 m, NOVA has $ASE-u=68\text{cm}$ and $ASE-o=81\text{cm}$, which is 65cm better than Geometric. Geometric also overestimates the distances by 251cm (false negative), which can be dangerous as the objects are closer than predicted. On the other hand, NOVA under-predicts for farther objects, estimating them to be nearer (false positive), which is relatively acceptable. For *scooters* (Fig. 18c), we observe a similar trend where Geometric model overestimates the distances for all 15 images, while NOVA overestimates only for 7 out of 15 images. For objects within 4 m, NOVA achieves an $ASE-o$ of just 1cm, demonstrating significantly higher accuracy. This extends to other classes like *cycle* (Fig. 18b) and *bystanders* (Fig. 18d). Here, the Geometric model overestimates distances for 100% of the images while NOVA limits this to 52% of images. NOVA also reduces absolute errors by up to 91cm for cycles and 114cm for bystanders for objects within 4 m, highlighting its better performance for closer objects

This is further validated in Fig. 19, where we summarize the over and underestimation errors for the most relevant quadrants, Q1, Q2, and Q3. Across all obstacle classes, NOVA demonstrates consistently lower errors or tends to underestimate distances (yellow shade). This is clearly evident in Q1 (Fig. 19a), where NOVA underestimates distances for all classes that have a ground truth distance that is farther off at 4 – 8 m. We focus on Q2 (Fig. 19b), which is key for our application as it has on objects within 4 m of the VIP (ground truth)

where the under-estimated distances are also within 4 m. Here, NOVA shows a significant improvement. When it overestimates (NOVA-o), the magnitude of its error is substantially lower compared to the Geometric model’s overestimation errors (Geo-o). E.g., for bystanders, NOVA’s error is $\approx 70\%$ lesser than Geo-o, ensuring better accuracy and safety during close-range navigation. Lastly, in Q3 (Fig. 19c), NOVA overestimates distances of near objects only for cycles and bystanders classes. Even here, the magnitude of error is much smaller compared to the Geometric model, further highlighting NOVA’s reliability.

Lastly, the median errors from SOTA methods ranges between 327 – 390 cm for MiDaS + ZoeDepth and 98 – 264 cm for Monodepth2.

Discussion. Overall, the results highlight NOVA’s ability to perform better compared to Geometric across multiple obstacle classes, particularly in critical scenarios where objects are within 4 m of the VIP. By significantly reducing the frequency and magnitude of overestimation errors and maintaining consistently lower error magnitudes across all quadrants, NOVA ensures safer and more reliable obstacle detection. These evidence make NOVA highly suitable for VIP use cases, as it enhances navigation safety and provides dependable obstacle avoidance, even in dynamic environments.

6.4 Time-varying errors for dynamic obstacles

In this section, we examine error across time in dynamic scenarios by analyzing one of the four dynamic videos in § 5.3.2. For the 206 secs long video where the VIP and drone are moving, and the stationary obstacles are stationary but moving relative to the drone camera in the scene; hence the same obstacle appear at different points in time at different distances. The temporal occurrence of obstacles are: bystander₁ at $t = 5s$, scooter at $t = 21s$, cycle at $t = 36s$, bystander₂ at $t = 49s$, bystander₃ at $t = 76s$ and car at $t = 88s$.

We evaluate the distance estimation methods: *Geometric* (Geo), *Geometric** (Geo*), NOVA without recalibration (NOVA-noRC), and NOVA with dynamic recalibration (NOVA-RC), against ground truth data. Fig. 20 illustrates the variation of signed errors (in meters, left Y-axis) over the video timeline (seconds) for the different obstacle classes encountered. We also report the ground truth distances to the obstacles from the drone (purple, right Y-axis). The regions shaded in gray background have the obstacle for that class at $> 4m$ from the drone, and hence are less critical for VIP navigation. The regions with red background have the obstacles within ≤ 4 from the drone, and are relevant for VIP navigation.

In Fig. 20a for the *car* class, both NOVA-noRC and NOVA-RC have a $\pm 1.1m$ error in the red region of proximity whereas the error for *Geometric* goes as high as $-3.0m$ and *Geometric** is slightly better at $-2.0m$ error. Both the *Geometric* models overestimate the distances for all classes and time-points. A similar trend is seen for other classes, where both variants of NOVA outperform. While the actual height of the car and scooter vary from the expected for *Geometric*, causing higher errors relative to *Geometric**, they are comparable for cycle and bystanders and the blue lines overlap. NOVA-RC performs comparable to NOVA-

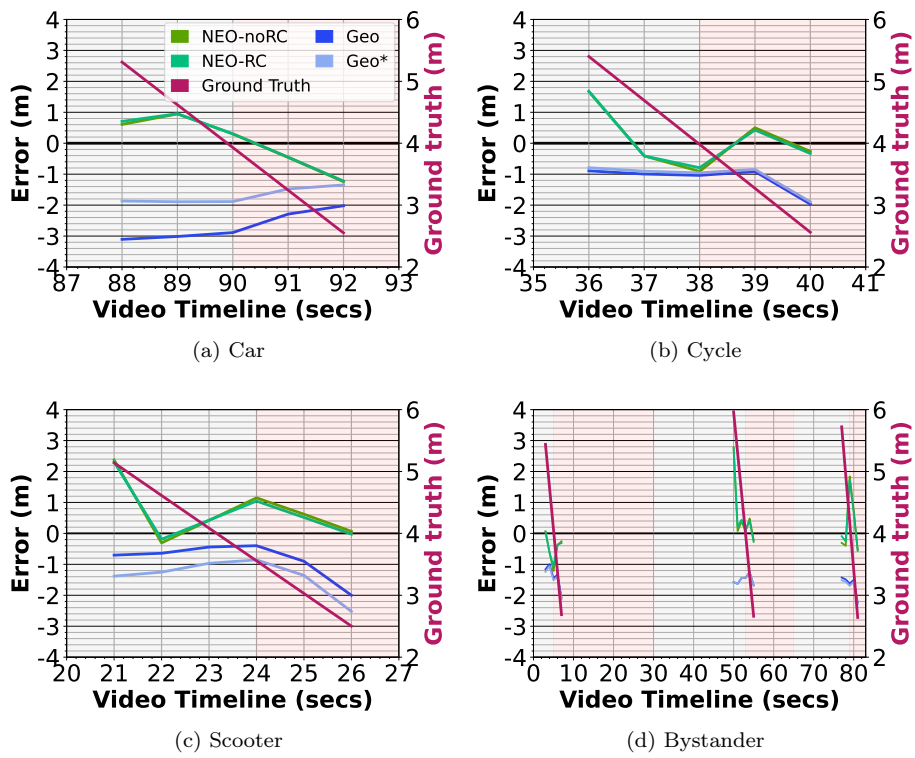


Figure 20: Error over time for objects, as VIP is moving

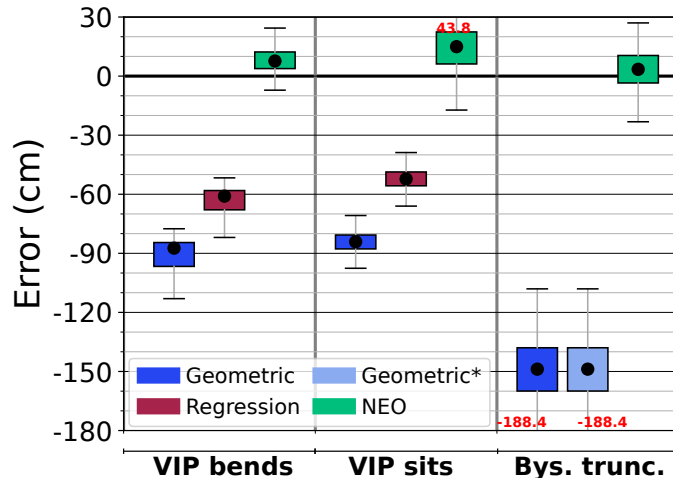


Figure 21: NOVA performs better for adversarial scenarios

noRC, and is marginally better in cycle and scooter for true distances $\leq 4m$. This would be even more prominent in adversarial scenes when NOVA-noRC does not recalibrate and NOVA-RC is able to adapt to dynamic scenarios.

Overall, we observe that both NOVA variants (NOVA-noRC and NOVA-RC) consistently outperform the Geometric and Geometric* methods across all obstacle classes and time points, particularly in critical proximity regions (red zones) where accurate distance estimation is vital for the VIP.

6.5 Robustness under adversarial scenarios

Lastly, we perform a focused evaluation of the proposed models on adversarial scenarios for the dataset listed in § 5.3.3 and Fig. 14. These challenging conditions cause the height of the YOLO bounding box to be incorrectly reduced for the VIP and bystander, and hence the distance estimates for Regression and Geometric, which are sensitive to the bounding box accuracy, are adversely affected. However, NOVA is able to predict the distances with a median error of $\leq 30cm$ in all cases, as shown in Fig. 21.

Here again, we observe significantly high median errors from SOTA methods in adversarial scenarios. Monodepth2 reports a minimum error of 201 cm, while MiDaS + ZoeDepth shows errors of ≥ 119 cm and goes as high as 245 cm.

We share a [supplementary video](#) to better visualize our evaluation results.

6.6 Discussion and Limitations

We summarize our observations of the benefits, limitations and overheads of the proposed methods in Table 4. For calibration and data collection, *Regression*

Table 4: Comparison summary of different methods

| METHOD | EFFORT | | ERROR FOR ADVERS. SCENES | | | | PROC. SPEED |
|----------------|------------------------------|--------------------------|-----------------------------|---------------------|---------------------------|------------------------|-------------|
| | <i>Calibration Over-head</i> | <i>Runtime Over-head</i> | <i>Varying Back-grounds</i> | <i>Orient-ation</i> | <i>Diff. Indi-viduals</i> | <i>Trunca-ted Obj.</i> | |
| Regres. | Medium | Low | Low | High | Low | High | Low |
| Geo | Low | Medium | Low | High | Low | High | Low |
| Geo* | Low | High | Low | High | Low | High | Low |
| NOVA | Medium | Low | Medium | Low | Low | Low | Low |

and NOVA have a MEDIUM overhead due to the need for calibration based on bounding box outputs from images. This requires manual effort in collecting ground truth distances for calibration. Geometric and Geo*, on the other hand, do not require any such calibration. Once the models are ready, Geo* requires the exact height of any object, which is a costly task; while Geo uses an average object height per class, incurring a MEDIUM overhead. Once calibrated, the other methods require no additional information.

On their robustness in adversarial scenarios, such as where the VIP changes their orientation by bending or sitting (Fig. 21), NOVA captures the correct distance estimates, whereas other methods fail because of their dependency on the bounding box parameters (height/width/area). Similarly, when objects get truncated due to their closeness to the camera, NOVA provides better results compared to other methods. However, the distance estimation of NOVA is affected by the lighting conditions or shiny surfaces.

All the methods generalize well across individuals. So, a model trained on one VIP will work equally well on any other VIP. Finally, as described in Table 2, all methods consume < 50ms of compute time on the edge accelerator.

7 Related Work

7.1 Vision-based Real-Time Obstacle Avoidance

Algorithms over images and videos have been used for collision avoidance. Early works such as Watanabe, et al. [38] use a single 2D passive vision sensor and extended Kalman filter (EKF) to estimate the relative position of obstacles using a collision-cone approach. Recent advances in machine perception, deep learning and GPU-accelerated computing have led to a large body of literature that integrate computer vision-based approaches with deep learning [39]. For these, obstacle avoidance is commonly vision-based, exploiting deep neural network (DNN) approaches to extract the navigation context from the scene [40]. We leverage some of these advances in our work.

Kaff et al. [23] propose an obstacle detection algorithm for UAVs equipped with monocular cameras, which analyzes changes in the pixel area of approaching obstacles. Obstacle avoidance is achieved by estimating the obstacle’s 2D

position in the image and combining it with tracked waypoints. Similarly, Lee et al. [24] utilize deep learning models for monocular obstacle avoidance in UAVs flying through tree plantations, classifying obstacles as critical or low priority based on the height of the bounding boxes around detected trees. However, these approaches are not designed to estimate absolute distances to objects, a crucial requirement for assisting visually impaired persons (VIPs) in navigation. Our work focuses on determining the distance to each object in the frame to classify them as obstacles and subsequently plan a collision-free path.

7.2 Depth-Map Based Navigation Techniques

Depth-map-based navigation techniques are widely used in autonomous systems for spatial awareness and obstacle detection [41]. Estimating a scene’s depth is very crucial, and integrating it with deep learning has shown success in achieving collision avoidance against moving obstacles and dynamic environments [42]. While stereo vision provide robust depth measurements under diverse lighting conditions and dynamic scenarios [43], monocular depth estimation has gained popularity as a cost-effective alternative due to its reliance on a single camera [44]. However, monocular approaches often struggle with accurately predicting absolute distances, relying heavily on relative depth cues [16, 20]. Additionally, the quality and accuracy of depth maps are highly sensitive to lighting conditions, with poor illumination or sharp shadows significantly degrading depth estimation performance. Unlike these methods, our proposed system, NOVA, focuses on estimating absolute distances using lightweight calibration techniques that dynamically adapt to changing scenes. This approach overcomes the limitations of purely monocular depth estimation by recalibrating depth coefficients in response to environmental variations, ensuring both adaptability and reliability for real-world navigation tasks.

Accurately estimating absolute distances from monocular views remains a core challenge without additional sensory inputs, such as stereo or LiDAR [44]. The DUEL (Depth visUal Ego-motion Learning) model combines depth perception with ego-motion estimation to enable autonomous robots to effectively avoid obstacles. However, its high computational demand limits its practical deployment [25]. Depth-map-based navigation techniques are increasingly being explored for edge-device deployments, particularly in UAVs and ground robots, to enable local processing of depth data. This approach minimizes latency and enhances real-time navigation [45]. An et al. [46] propose a low-complexity network optimized for fast human depth estimation and segmentation in indoor environments, tailored for resource-constrained edge devices. Building on these efforts, NOVA focuses on outdoor applications and leverages NVIDIA Jetson-series edge devices to dynamically recalibrate, while still achieving real-time performances.

7.3 Absolute Distance Estimation Methods

Absolute distance estimation is a critical component in robotics and autonomous navigation. Traditional methods, such as stereo vision and LiDAR, directly measure distances based on geometric triangulation or light reflection times, providing high accuracy in estimating absolute distances but often requiring expensive hardware and significant processing power [47]. SOTA methods for distance estimation integrate camera feeds with LiDAR [48] or use RGB-D cameras [49] to generate a 3D view of the surroundings. We limit ourselves to just monocular images from the UAV camera to ensure wider applicability using affordable consumer drones.

In monocular vision systems, there is an *inherent scale ambiguity* where the actual size and distance of objects cannot be distinguished. This makes it challenging to gauge the true depth without assumptions about object size or additional sensors for distance verification [50]. We observe a similar issue while evaluating our baseline *Geometric* method that estimates the distance to an object using only the average height of the object class as input and demonstrates that the estimation errors increase when the VIP is partially out of the frame or if the object size estimations are skewed from the actual sizes. NOVA with its calibration techniques adapts well to such variations.

Further, deep reinforcement learning using monocular vision [42] and end-to-end learning have also been implemented for autonomous vehicles [51], but require massive training datasets. Some use geometric methods [52] on static objects but need details on the road geometry and point of contact on the road. We instead focus on lightweight methods that operate on monocular images with minimal ancillary metadata, and attempt to generalize to any object perceived by the UAV.

8 Conclusion and Future Work

In this paper, we proposed a novel approach, NeoARCADE (NOVA), which leverages depth maps to estimate absolute distances to obstacles in outdoor urban environments, facilitating obstacle detection and eventually autonomous navigation for VIPs. NOVA uses robust calibration methods to address the limitations of SOTA depth map approaches like MiDaS and MonoDepth2, which offer poor accuracy for real distances. Additionally, we present Geometric and Regression-based methods along with their calibration techniques as baselines. We evaluate their efficacy on diverse videos at various distances, backgrounds and complex environments in outdoor campus settings, captured using a DJI Tello drone. While Regression calibrated on specific VIPs works best for the VIP’s distance estimate, NOVA performs consistently better for all other obstacles, scales well to dynamic changes, and outperforms in adversarial conditions.

As future work, we plan to integrate these with path-planning algorithms for the local navigation of the VIPs. Also, the depth map methods require further investigation to enhance their accuracy, which will be explored in future work.

Additionally, we plan to extend this approach to experiments in other complex scenarios with dynamic obstacles emulating real-time use cases to provide enhanced collision avoidance guidance to VIPs and the drone.

References

- [1] A. Momont, “[Ambulance Drone at TU Delft](#),” TUDelft, Tech. Rep., 2014.
- [2] A. Ollero, J. Ferruz, F. Caballero, S. Hurtado, and L. Merino, “Motion compensation and object detection for autonomous helicopter visual navigation in the comets system,” in *IEEE ICRA*, 2004.
- [3] A. Santamaria-Navarro, R. Thakker, D. D. Fan, B. Morrell, and A.-a. Agha-mohammadi, “Towards resilient autonomous navigation of drones,” in *Robotics Research*. Springer International, 2022.
- [4] A. Gupta and X. Fernando, “Simultaneous localization and mapping (slam) and data fusion in unmanned aerial vehicles: Recent advances and challenges,” *Drones*, vol. 6, no. 4, 2022. [Online]. Available: <https://www.mdpi.com/2504-446X/6/4/85>
- [5] M. Y. Arafat, M. M. Alam, and S. Moh, “Vision-based navigation techniques for unmanned aerial vehicles: Review and challenges,” *Drones*, 2023.
- [6] S. Raj, H. Gupta, and Y. Simmhan, “Scheduling dnn inferencing on edge and cloud for personalized uav fleets,” in *IEEE/ACM CCGrid*, 2023.
- [7] B. Kuriakose, R. Shrestha, and F. E. Sandnes, “Tools and technologies for blind and visually impaired navigation support: a review,” *IETE Technical Review*, vol. 39, no. 1, pp. 3–18, 2022.
- [8] M. Al Zayer, S. Tregillus, J. Bhandari, D. Feil-Seifer, and E. Folmer, “Exploring the use of a drone to guide blind runners,” in *ACM SIGACCESS*, 2016.
- [9] W. H. Organization, “[Blindness and visual impairment fact sheets](#),” WHO, Tech. Rep., August 2023.
- [10] S. Raj, S. Padhi, and Y. Simmhan, “Ocularone: Exploring drones-based assistive technologies for the visually impaired,” in *Extended Abstracts, ACM SIGCHI*, 2023.
- [11] “WeWALK Smart Cane: Enhancing the Mobility of the Visually Impaired,” <https://wewalk.io/en/>, accessed: 2025-01-05.
- [12] J. Bai, S. Lian, Z. Liu, K. Wang, and D. Liu, “Smart guiding glasses for visually impaired people in indoor environment,” *IEEE Transactions on Consumer Electronics*, 2017.

- [13] A. Al-Heeti, “Google expands lookout app for people who are blind or vision-impaired,” CNet, Tech. Rep., Aug. 2020.
- [14] M. M. Nasralla, I. U. Rehman, D. Sobnath, and S. Paiva, “Computer vision and deep learning-enabled uavs: proposed use cases for visually impaired people in a smart city,” in *CAIP*, 2019.
- [15] M. Avila Soto, M. Funk, M. Hoppe, R. Boldt, K. Wolf, and N. Henze, “Dronenavigator: Using leashed and free-floating quadcopters to navigate visually impaired travelers,” in *ACM SIGACCESS*, 2017.
- [16] D. Eigen, C. Puhrsch, and R. Fergus, “Depth map prediction from a single image using a multi-scale deep network,” *Advances in neural information processing systems*, vol. 27, 2014.
- [17] D. G. Low, “Distinctive image features from scale-invariant keypoints,” *Journal of Computer Vision*, vol. 60, no. 2, pp. 91–110, 2004.
- [18] A. Kendall, H. Martirosyan, S. Dasgupta, P. Henry, R. Kennedy, A. Bachrach, and A. Bry, “End-to-end learning of geometry and context for deep stereo regression,” in *Proceedings of the IEEE international conference on computer vision*, 2017, pp. 66–75.
- [19] R. Ranftl, K. Lasinger, D. Hafner, K. Schindler, and V. Koltun, “Towards robust monocular depth estimation: Mixing datasets for zero-shot cross-dataset transfer,” *IEEE transactions on pattern analysis and machine intelligence*, 2020.
- [20] C. Godard, O. Mac Aodha, M. Firman, and G. J. Brostow, “Digging into self-supervised monocular depth prediction,” in *The International Conference on Computer Vision (ICCV)*, October 2019.
- [21] S. F. Bhat, R. Birkl, D. Wofk, P. Wonka, and M. Müller, “Zoedepth: Zero-shot transfer by combining relative and metric depth,” 2023. [Online]. Available: <https://arxiv.org/abs/2302.12288>
- [22] R. Ranftl, A. Bochkovskiy, and V. Koltun, “Vision transformers for dense prediction,” *IEEE International Conference on Computer Vision (ICCV)*, pp. 12 179–12 188, 2021.
- [23] A. Al-Kaff, F. García, D. Martín, A. De La Escalera, and J. M. Armingol, “Obstacle detection and avoidance system based on monocular camera and size expansion algorithm for uavs,” *Sensors*, 2017.
- [24] H. Lee, H. W. Ho, and Y. Zhou, “Deep learning-based monocular obstacle avoidance for unmanned aerial vehicle navigation in tree plantations: Faster region-based convolutional neural network approach,” *Journal of Intelligent & Robotic Systems*, 2021.

- [25] N. Wang, B. Zhang, H. Chi, H. Wang, S. McLoone, and H. Liu, “Duel: Depth visual ego-motion learning for autonomous robot obstacle avoidance,” *The International Journal of Robotics Research*, vol. 43, no. 3, pp. 305–329, 2024.
- [26] X. Peng, Z. Liu, W. Li, P. Tan, S. Y. Cho, and Q. Wang, “Dvi-slam: A dual visual inertial slam network,” in *2024 IEEE International Conference on Robotics and Automation (ICRA)*, 2024, pp. 12 020–12 026.
- [27] A. Geiger, P. Lenz, and R. Urtasun, “Kitti vision benchmark suite: Raw data,” https://www.cvlibs.net/datasets/kitti/raw_data.php, 2012, accessed: 2025-01-05.
- [28] M. Cloutier and P. R. DeLucia, “Topical review: Impact of central vision loss on navigation and obstacle avoidance while walking,” *Optometry and Vision Science*, vol. 99, no. 12, pp. 890–899, 2022.
- [29] G. Jocher, A. Chaurasia, and J. Qiu, “Ultralytics yolov8,” 2023. [Online]. Available: <https://github.com/ultralytics/ultralytics>
- [30] P. Sturm, *Pinhole Camera Model*. Boston, MA: Springer US, 2014. [Online]. Available: https://doi.org/10.1007/978-0-387-31439-6_472
- [31] R. I. Hartley and A. Zisserman, *Multiple View Geometry in Computer Vision*, 2nd ed. Cambridge University Press, 2004.
- [32] S. F. Bhat, I. Alhashim, and P. Wonka, “Adabins: Depth estimation using adaptive bins,” in *Proceedings of the IEEE/CVF conference on computer vision and pattern recognition*, 2021, pp. 4009–4018.
- [33] B. Yu, J. Wu, and M. J. Islam, “Udepth: Fast monocular depth estimation for visually-guided underwater robots,” in *2023 IEEE International Conference on Robotics and Automation (ICRA)*. IEEE, 2023, pp. 3116–3123.
- [34] B. Ke, A. Obukhov, S. Huang, N. Metzger, R. C. Daudt, and K. Schindler, “Repurposing diffusion-based image generators for monocular depth estimation,” in *Proceedings of the IEEE/CVF Conference on Computer Vision and Pattern Recognition (CVPR)*, 2024.
- [35] I. Alhashim and P. Wonka, “High quality monocular depth estimation via transfer learning,” *arXiv e-prints*, vol. abs/1812.11941, 2018. [Online]. Available: <https://arxiv.org/abs/1812.11941>
- [36] R. Tech, “RYZE Tello: Powered by DJI,” 2018.
- [37] N. Developer, “Jetson Orin Nano Developer Kit,” 2023.
- [38] Y. Watanabe, A. Calise, and E. Johnson, “Vision-based obstacle avoidance for uavs,” in *AIAA guidance, navigation and control conference and exhibit*, 2007, p. 6829.

- [39] L. Mejias, S. McNamara, J. Lai, and J. Ford, "Vision-based detection and tracking of aerial targets for uav collision avoidance," in *IEEE/RSJ International Conference on Intelligent Robots and Systems*, 2010.
- [40] A. Loquercio, E. Kaufmann, R. Ranftl, M. Müller, V. Koltun, and D. Scaramuzza, "Learning high-speed flight in the wild," *Science Robotics*, vol. 6, no. 59, p. eabg5810, 2021.
- [41] H. Müller, V. Niculescu, T. Polonelli, M. Magno, and L. Benini, "Robust and efficient depth-based obstacle avoidance for autonomous miniaturized uavs," *IEEE Transactions on Robotics*, 2023.
- [42] X. Liu, Z. Zhu, and H. Zhang, "Deep reinforcement learning for navigation of uavs with obstacle avoidance," *IEEE Access*, vol. 7, pp. 156 720–156 732, 2019.
- [43] J. Zhang, X. Wang, and L. Xie, "Stereo depth estimation network for real-time stereo vision applications," *IEEE Transactions on Industrial Electronics*, vol. 67, no. 11, pp. 9392–9402, 2020.
- [44] H. Fu, M. Gong, C. Wang, K. Batmanghelich, and D. Tao, "Deep ordinal regression network for monocular depth estimation," in *Proceedings of the IEEE conference on computer vision and pattern recognition*, 2018, pp. 2002–2011.
- [45] C. Sampedro, H. Bavle, A. Carrio, and P. Campoy, "Uav autonomous navigation and obstacle avoidance using depth maps and artificial potential fields," *IEEE Robotics and Automation Letters*, vol. 3, no. 4, pp. 3271–3278, 2018.
- [46] S. An, F. Zhou, M. Yang, H. Zhu, C. Fu, and K. A. Tsintotas, "Real-time monocular human depth estimation and segmentation on embedded systems," in *2021 IEEE/RSJ International Conference on Intelligent Robots and Systems (IROS)*, 2021, pp. 55–62.
- [47] R. Szeliski, *Computer vision: algorithms and applications*. Springer Nature, 2022.
- [48] Z. Li, P. C. Gogia, and M. Kaess, "Dense surface reconstruction from monocular vision and lidar," in *ICRA*, 2019.
- [49] M. Iacono and A. Sgorbissa, "Path following and obstacle avoidance for an autonomous uav using a depth camera," *Robotics and Autonomous Systems*, vol. 106, pp. 38–46, 2018.
- [50] R. Mur-Artal and J. D. Tardós, "Orb-slam2: An open-source slam system for monocular, stereo, and rgb-d cameras," *IEEE Transactions on Robotics*, vol. 33, no. 5, pp. 1255–1262, 2017.

- [51] M. Bojarski, D. Del Testa, D. Dworakowski, B. Firner, B. Flepp, P. Goyal, L. D. Jackel, M. Monfort, U. Muller, J. Zhang, *et al.*, “End to end learning for self-driving cars,” *arXiv:1604.07316*, 2016.
- [52] A. Joglekar, D. Joshi, R. Khemani, S. Nair, and S. Sahare, “Depth estimation using monocular camera,” *International journal of computer science and information technologies*, 2011.